





# Extruded TOPAS hollow-core anti-resonant fiber optimized for THz guidance at 0.9THz

NATTHAWAT PHANCHAT,<sup>1,2,\*</sup>  WANVISA TALATAISONG,<sup>1,3</sup>   
NICHOLAS KLOKKOU,<sup>1</sup>  RATCHAPAK CHITAREE,<sup>2</sup> VASILIS  
APOSTOLOPOULOS,<sup>4</sup>  MARTYNAS BERESNA,<sup>1</sup>  AND GILBERTO  
BRAMBILLA<sup>1</sup> 

<sup>1</sup>Optoelectronics Research Centre, University of Southampton, Southampton SO17 1BJ, UK

<sup>2</sup>Applied Optics Research Group, Department of Physics, Faculty of Science, Mahidol University, Bangkok 10400, Thailand

<sup>3</sup>School of Physics, Suranaree University of Technology, Nakhon Ratchasima 30000, Thailand

<sup>4</sup>School of Physics and Astronomy, University of Southampton, Southampton SO17 1BJ, UK

\*n.phanchat@soton.ac.uk

**Abstract:** A hollow-core anti-resonant fiber for the THz regime is proposed and demonstrated. The proposed fiber is the hexagonal core shape which is directly extruded using a conventional 3D printer. Experimental results show that by using cyclic olefin copolymer (COC), the proposed fiber design provides a low attenuation of  $\sim 3$  dB/m at  $\sim 0.86$  THz and  $\sim 15$  dB/m at  $\sim 0.42$  THz.

Published by Optica Publishing Group under the terms of the [Creative Commons Attribution 4.0 License](https://creativecommons.org/licenses/by/4.0/). Further distribution of this work must maintain attribution to the author(s) and the published article's title, journal citation, and DOI.

## 1. Introduction

Terahertz (THz) waves with frequency in the range  $f \sim 0.1$ – $10$  THz (corresponding to the free-space wavelength range  $\lambda \sim 3.00$ – $0.03$  mm) have found many applications due to their unique properties, including non-ionizing nature and deep penetration in most of materials. This allows inspecting organic tissues without causing damage and can be applied to medical and biomedical sensing. In addition, the wavelength of THz waves is shorter than microwaves, thus offering superior image resolution [1–4]. THz waves are also gaining popularity for detecting chemical, pharmaceutical and biological agents due to the molecule distinctive features in this spectral region [5–10]. In astronomy, THz can be used to locate cold matter in space or for imaging applications in deep space [11]; while in wireless communications they have the potential to increase data transmission due to the large bandwidth of the THz band [12,13].

In the past decade, many researchers attempted to design and fabricate waveguides for THz guidance paving the way to integrated THz systems and related applications such as imaging, microscopy, quantum-cascade lasers [14], monitoring of chemical reactions [15] and medical endoscopy of internal organs [16]. Most of the research has focused on optimizing the transmission and minimizing the dispersion of THz waveguides. To achieve low-loss waveguides, the material used for fiber fabrication plays an important role because of its absorption.

As vacuum and air represent the lowest absorption media, THz pipe waveguides have been proposed for low-loss propagation because of the large fraction of mode propagating in air and the relatively simple structure: in 2010 a record low loss  $\sim$ of  $0.0005$   $\text{cm}^{-1}$  ( $\sim 0.2$  dB/m) was demonstrated in a 15-cm long [17] with 3% oscillation in the wall thickness. Yet, the transmission window of these waveguides is limited by the tube wall thickness. Thin wall tubes are difficult to fabricate, handle and cleave, and the resulting pipe waveguide is fragile and sensitive to external perturbations.

Polymer waveguides have been proposed because of their ease of manufacture, low material cost, robustness and insensitivity to the external environment. The first low-loss THz polymer waveguide, proposed in 2000, used high-density polyethylene (HDPE) [18]. Two years later, HDPE was used to fabricate a THz-guiding microstructured polymer optical fiber, which exhibited a minimum attenuation of  $0.5 \text{ cm}^{-1}$  [19]. Polytetrafluoroethylene (PTFE, or Teflon) is another polymer with low attenuation in the THz range: in 2004, a Teflon THz fiber with  $0.1 \text{ cm}^{-1}$  attenuation was demonstrated [20].

TOPAS (cyclic olefin copolymer), a commercial thermoplastic, has also been suggested as a material of choice for THz waveguides due to its low material attenuation at THz frequencies. TOPAS can be exploited for various types of fibers, such as a suspended porous microstructured fiber, hybrid core porous THz fiber and hollow-core anti-resonant fiber [21,22]. In 2009, TOPAS optical fibers were fabricated for guidance at  $f \sim 0.1\text{--}3 \text{ THz}$  [23]. In 2013, hollow-core terahertz photonic crystal fibers made of TOPAS were designed and fabricated for operating at  $f \sim 0.6 \text{ THz}$  with a reported attenuation of  $0.75 \text{ dB/m}$  [24]. Hollow core fibers exhibit the benefits of both polymer and pipe waveguides, as their thin core perimetral wall allows for a relatively large transmission window, while the external thick cladding wall provides stiffness and isolation from the surrounding environment. Simulations showed that a loss of  $2.1 \text{ dB/m}$  can be achieved at  $1.2 \text{ THz}$  [25]. Recently, a commercial 3D printer has been proposed for fiber fabrication, as it is easy in terms of fiber preparation, and also cheaper than the traditional techniques [26]. The fabrication of a TOPAS suspended-core THz fiber based on 3D printer by using a modified structured nozzle has been reported in 2019. This fiber could operate in the range of  $0.5 - 1.0 \text{ THz}$  with the loss of  $\sim 110 \text{ dB/m}$  [27]. By using the same technique, a hollow-core anti-resonant THz fiber-based TOPAS was fabricated in 2021. This fiber was directly extruded in a single-step procedure using a conventional 3D printer. The desired geometry of the fiber was achieved by using a customized nozzle. The fiber could be used for guidance in the range  $f \sim 0.4\text{--}1.0 \text{ THz}$  with a minimum attenuation of  $12 \text{ dB/m}$  at  $f \sim 0.7 \text{ THz}$  [28].

In this paper we exploit the flexibility of this manufacturing process to improve the fiber performance of a hollow core TOPAS fiber. Simulations based on the finite element method (FEM) with a perfectly matched layer (PML) boundary have been used to investigate the loss profile of the fundamental core mode: by increasing the core size and decreasing the struts thickness, the fiber attenuation improves, while the transmission window increases. A nozzle designed using an optimized simulation model was 3D-printed and used for the fiber fabrication. The resulting fiber exhibited a record low loss for a polymer suspended hollow core fiber of  $2 \text{ dB/m}$  at  $0.85 \text{ THz}$ .

## 2. Anti-resonant guidance

Hollow-core anti-resonant fibers exploit a single wall or multiple walls surrounding the core region for guidance. The wall thickness and material are the main factors to determine the wavelengths (called “anti-resonant wavelengths”) that can be confined in the core region.

The fiber wall, which acts as a cladding of this fiber structure, can be considered as a Fabry-Perot resonator: for specific wavelengths, matching the anti-resonant condition, the fiber experiences low leakage because of the destructive interference of the Fabry-Perot resonator. For a fiber with multiple walls, each wall is also considered as an individual Fabry-Perot resonator, and the leakage is better controlled, thus lower, than that for a single wall.

Theoretically, the maximum leakage (high loss) located at the resonance frequency ( $f_r$ ) can be calculated by the following formula [29–31]:

$$f_r = \frac{mc}{2t\sqrt{n_{mat}^2 - n_{air}^2}} \quad (1)$$

where  $c$  is the speed of light in vacuum,  $m$  is an integer,  $n_{mat}$  is the refractive index of the fiber material,  $n_{air}$  is the refractive index of fiber core (air), and  $t$  is the thickness of the core perimetral wall.

Light confinement occurs in the window between the resonance frequencies, and transmission is critically affected by the imperfect reflections at the low-high index interfaces.

### 3. Modelling and simulation results

Although in previous works, PE [32], high-density polyethylene (HDPE) [19], teflon [20], Zeonex [33] and cyclic olefin copolymer (COC) or TOPAS [23,34–37] have all been proposed for THz guidance, TOPAS has attracted most attention due to its low material absorption, low dispersion in the THz spectral range [27,28], and a glass-transition temperature of  $\sim 200^\circ\text{C}$ , making it particularly suitable for using with commercial fused deposition modelling 3D printers [38]. TOPAS also exhibits high moisture barrier along with a low moisture absorption rate [39]. These properties are essential for THz guidance because moisture affects transmission efficiency.

The filament used in this work was produced by the Institute for Material Science and Plastic Processing, Eastern Switzerland University of Applied Sciences, Switzerland. The glass-transition and melting temperatures of the used material were  $T_g \sim 185^\circ\text{C}$  and  $T_m \sim 250^\circ\text{C}$ , respectively; the refractive index was  $n \sim 1.54$  at  $f \sim 0.1\text{--}1.5$  THz.

The proposed hollow-core anti-resonant fiber includes a hexagonal shaped hole located at the center of the fiber, which is surrounded by a thin hexagonal wall suspended by six struts that connect the hexagonal wall to the outer shell (Fig. 1(a)). In the design optimization process, the fiber hexagonal wall thickness, core diameter and struts thickness were considered [28]. The overall fiber diameter and outer shell thickness were limited by the power provided by the 3D printer heater and were set at 8, and 1 mm. The struts length was varied with the fiber core diameter. To optimize the loss of the fiber, the core diameter was varied between 2.00–3.80 mm, while three different core thickness values ( $t = 0.35$  mm, 0.50 mm and 0.65 mm) were selected. These three values were the optimal values for operation at  $f \sim 0.8\text{--}1.0$  THz.

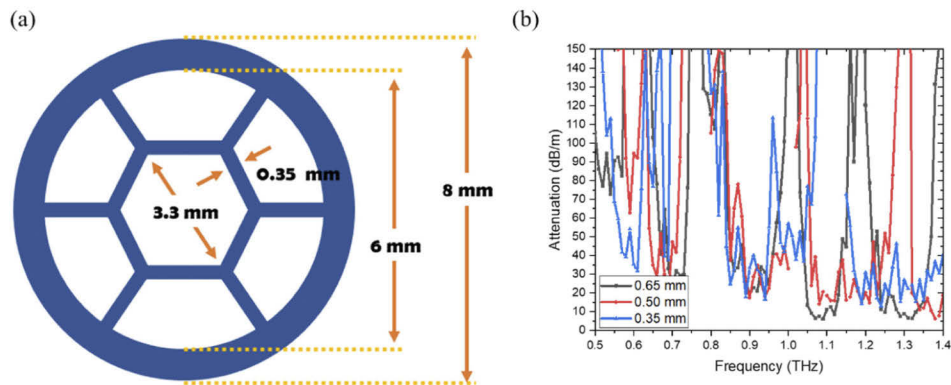


**Fig. 1.** (a) Schematic diagram of the proposed fiber cross-section. (b) Confinement loss as a function of frequency for different values of  $t$  (wall thickness).

The Finite Element Method (FEM) based COMSOL Multiphysics software was used to design the hollow-core anti-resonant fiber and evaluate its attenuation. In order to obtain maximum accuracy in the simulations, a user-controlled mesh type with extremely fine mesh size ( $\lambda/15$  for core region,  $\lambda/6$  for cladding region) was selected, while a perfectly matched layer (PML), was used as external layer, which acted as an anti-reflection layer. The confinement loss ( $L_c$ ) of the

proposed fiber was evaluated using [40]:

$$L_c = 8.686 \left( \frac{2\pi f}{c} \right) \text{Im}(n_{eff}) \text{ [dB/m]} \quad (2)$$

where  $c$  is the speed of light in vacuum, and  $\text{Im}(n_{eff})$  the imaginary part of the complex effective refractive index.

### 3.1. Perimetral wall thickness

Three different values of perimetral wall thickness  $t$  were chosen for optimal operation at  $f \sim 0.9$  THz ( $t = 0.35$  mm, 0.50 mm and 0.65 mm), while the operating frequency was swept from  $f = 0.50$  THz to  $f = 1.40$  THz in 0.01 THz steps. The simulation results in Fig. 1(b) indicate that the confinement loss at  $f \sim 0.85$ -0.95 THz is not significantly affected by variation of  $t$ , but fluctuations can be clearly observed. For  $t = 0.65$  mm, the fluctuations in the anti-resonant region are small, but the low-attenuation region is rather narrow. For  $t \sim 0.35$  mm, low-attenuation propagation occurs over a wider bandwidth, but at the expense of larger fluctuations.

For a wider guiding region, the thickness of core surround of 0.35 mm was chosen.

### 3.2. Strut thickness

A significant contribution to the attenuation in the fiber core comes from the connecting region between the core perimetral wall and the supporting struts. At this region, the membrane does not behave as an etalon (two parallel reflectors), resulting in an overall small reflection of the guided wave into the fiber core, and an increased leakage into the cladding. By optimizing the thickness of the struts ( $h$ ), the confinement loss can be reduced. Three strut thicknesses were chosen:  $h = 0.35$  mm, 0.50 mm and 0.65 mm. The core perimetral wall thickness for each design was fixed at  $t = 0.35$  mm.

Figure 2(a) shows the simulation results of the fiber attenuation [dB/m] as a function of the operating frequency for  $f = 0.50$ -1.40 THz for the three strut thicknesses. The red shade represents the resonant region of high loss.

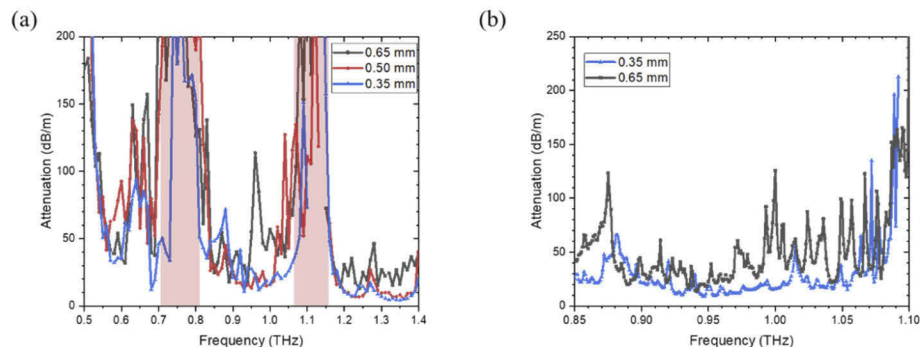


**Fig. 2.** Confinement loss (a) for different values of strut thickness in the region  $f = 0.5$ -1.4 THz, and (b) details in the region  $f = 0.85$ -1.1 THz for 0.35 mm and 0.65 mm of the strut thickness.

These results show that the fiber with  $h = 0.35$  mm has a narrow resonant region, with an estimated width of  $\sim 0.08$  THz, while that with  $h = 0.65$  mm provides a resonant width two times larger. The change of  $h$  also affects the attenuation profile in the anti-resonant region: Fig. 2(b) shows that in the region  $f \sim 0.85$  - 1.10 THz the model with  $h = 0.65$  mm has more fluctuations than the model with  $h = 0.35$  mm. Thickness  $t = 0.35$  mm and height  $h = 0.35$  mm are therefore chosen for further optimization of the confinement losses.

The fluctuations in the attenuation curve are related to the hexagonal geometry of the fiber, and in particular to the six struts connecting the thin membrane surrounding the fiber core with the fiber cladding. Fiber guidance is based on the anti-resonant effect at the two parallel interfaces surrounding the fiber core (thin membrane). The corners around the hexagonal core cannot maintain the resonant condition, and this results in a leak of the confined more mode.

### 3.3. Core diameter

As the fiber outer and inner shell diameters are fixed at 8.00 and 6.00 mm, the core diameter  $D$  is varied from 2.00 mm to 3.80 mm in this further optimization process step (Fig. 3(a)). The loss is extremely high for  $D < 2.00$  mm, while it gradually decreases for increasing core diameters. Figure 3(a) shows that the optimum core diameter is  $D \sim 3.30$  mm, which theoretically provides a loss lower than 5 dB/m at 0.90 THz.

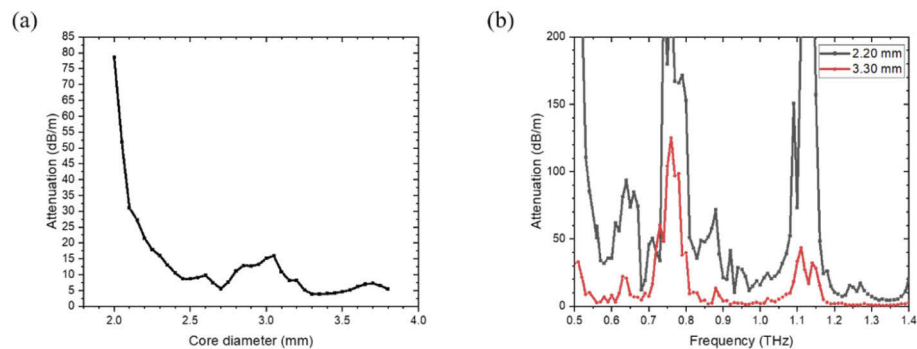


**Fig. 3.** (a) Confinement loss as a function of the core diameter  $D$  at 0.90 THz. (b) Confinement loss as a function of frequency for  $D = 2.20$  mm (black) and  $D = 3.30$  mm (red);  $h = t = 0.35$  mm.

The spectral attenuation, calculated for these optimized parameters ( $D = 3.30$  mm,  $t = 0.35$  mm and  $h = 0.35$  mm), is shown in Fig. 3(b) and compared to a smaller core size ( $D = 2.2$  mm).

The two models have the same resonant regions due to the same core perimetral wall thickness. Yet, the attenuation profile of the fiber with larger core is lower than that with  $D = 2.20$  mm, because of the smaller mode/material overlap. The fiber with  $D = 3.30$  mm also provides smoother frequency response in the range  $f = 0.85 - 1.05$  THz.

## 4. Fabrication of an optimized hollow-core anti-resonant fiber

### 4.1. Nozzle fabrication

The drawing system demonstrated by Talataisong et al. [27,28] was used to manufacture the fiber with the optimized design. The dimensions of the structured nozzle were based on the general size of the commercial 3D printer nozzle, which has a 6 mm thread diameter. The diameter of the polymer filament used in this experiment was 2.85 mm, while the designed nozzle had a 3.5 mm aperture diameter at the input, where the polymer was fed into the nozzle. The optimized parameter from the simulation were used to design the inner structure of the nozzle which had a hexagonal rod with  $D = 3.30$  mm located at the center of the nozzle. The gaps between the central hexagonal rod and the six surrounding neighboring rods around the core have the thickness of  $t \sim h \sim 0.35$  mm, as they produce the core perimetral wall and struts. The outer ring gap was 1.00 mm and produced the outer layer of the extruded optical fiber. The optimized nozzle was manufactured with a metal 3D printer and is shown in Fig. 4(a).



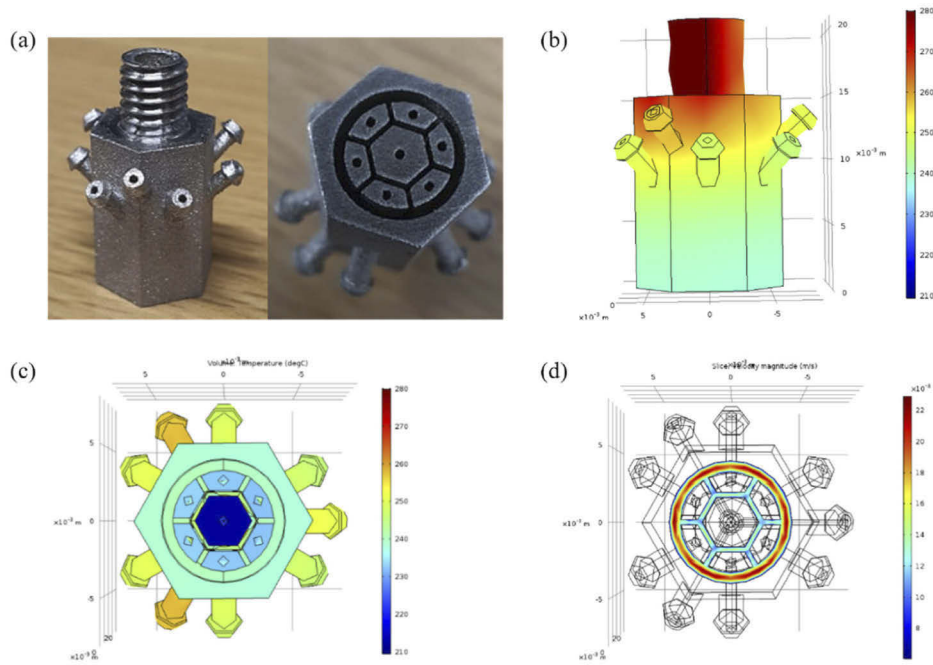


**Fig. 4.** (a) Metal 3D printed structured nozzle. (b, c) Heat transfer simulations of the designed nozzle when applied temperature at 280 °C to the nozzle thread; (b) side view and (c) bottom view. (d) Material flow simulation of the designed nozzle when a temperature of 280°C was applied at the nozzle thread and the material feeding speed was set at 18 mm/min.

As the outer ring is much thicker than internal struts, the polymer flow can be potentially disrupted due to different in flow resistance. The heat transfer and the material flow were simulated using COMSOL to optimize the structured nozzle inner structure and length. Figure 4(b, c) shows the heat transfer simulations for a 22 mm long stainless-steel nozzle fabricated, and indicate that the temperature at the nozzle extrusion end is reduced from the applied temperature of 280°C to 210°C. The lowest temperature at the fiber end is higher than the glass-transition temperature of TOPAS, confirming the possibility to use this nozzle design as a die for the fiber extrusion. The material flow simulations (Fig. 4(d)) confirm that there is a material flowing through the gap regions.

#### 4.2. Fiber fabrication

The TOPAS THz fiber was extruded from the heated structured nozzle. Initial draws produced a fiber with decreasing diameter for increasing fiber lengths. This was attributed to the increasing amount of the material present after the die output for increasing fiber lengths, which result in an increasing gravitational force acting on the least viscous section of the fiber. To avoid this problem, a support was applied at the bottom of the extruded fiber, specifically designed to move synchronously with the fiber.

Figure 5(a) shows the fiber diameter at different fiber lengths with and without support. Without support, the fiber diameter decreased for increasing lengths, while with support, the fiber diameter remained stable. The support got in touch with the extruded fiber at the length 8 cm, after which they moved together.

In the fiber fabrication process, the nozzle temperature was set at the applied temperature of 280 °C. The TOPAS polymer was fed through the heated nozzle with a feeding speed of 18

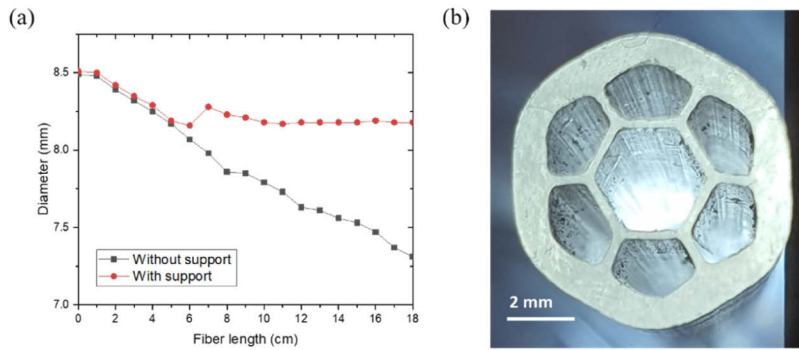


**Fig. 5.** (a) Fiber diameter as a function of fiber length from fibers drawn with and without support. (b) Cross-section of the TOPAS hollow-core anti-resonant THz fiber.

mm/min resulting in a fiber extruding speed of 0.6 mm/s. The cross-section of the extruded fiber is shown in Fig. 5(b).

The parameters from extruded fiber are slightly smaller than the proposed model. The air core diameter was found to be  $D \sim 3.10$  mm, the core thickness and the strut thickness were found to be  $t = h \sim 0.25$  mm. The whole fiber diameter is slightly bigger than the proposed model, which is 8.19 mm. The slight mismatch between the extruded fiber and the proposed model comes from the ununiform material speed when extruding the fiber. The material flow simulation (Fig. 4(d)) shows that the material speed in the outer shell region is higher than in the hexagonal wall and struts regions. The higher speed becomes thicker than other parts.

## 5. Fiber characterization

To confirm guidance in the THz region, the fiber was characterized by using THz time-domain spectroscopy (TDS) [41]. In the experiment, a signal of THz beam passing through the air was collimated by a pair of polymethyl pentene (TPX) lenses. With optical fiber, two additional TPX convex lenses were used to focus the THz beam into the fiber core.

The continuous wavelet transform was used to analyze the signal from the time domain to the frequency domain by Fourier transform with an auto-selected sample window. The magnitude scalogram of the collimated beam is presented in Fig. 6(a). The color represents the magnitude of the transmission signal, showing that the THz source emitter is active at  $f \sim 0.1$ -1.1 THz and it has a very strong intensity around  $f \sim 0.3$  THz. The magnitude scalogram of the THz wave guided in the 30 mm of HC-ARF is shown in Fig. 6(b). The anti-resonant frequencies can be clearly observed when compared with the collimated beam, showing that the fiber has 2 anti-resonant windows at  $f \sim 0.28$ -0.52 THz and at  $f \sim 0.65$ -0.95 THz.

The transmission signals were Fourier transformed and presented in the frequency domain in Fig. 6(c): the frequency-domain spectrum of the THz wave from the THz emitter is shown in black, while the transmission spectrum of the THz wave guided in 30 mm of HC-ARF is in blue. The transmission spectrum of the fiber shows that the anti-resonant windows can be observed, which is highlighted as a light green area. Between the anti-resonant windows, the amplitude of the transmission spectrum drops dramatically due to high loss at the resonant frequencies.

Figure 6(c) shows that the Fourier transform of the raw signal exhibits a significant noise level. The use of time gating with the signal can reduce the noise when using Fourier transform, thus a Gaussian curve is applied as time window for filtering out the noise. The signal magnitude scalogram obtained from wavelet transform clearly allows to determine the position and width of a signal time window, and it has been applied to the raw signal before Fourier transform. The time that provided the maximum magnitude in the scalogram is used as the center, and the full

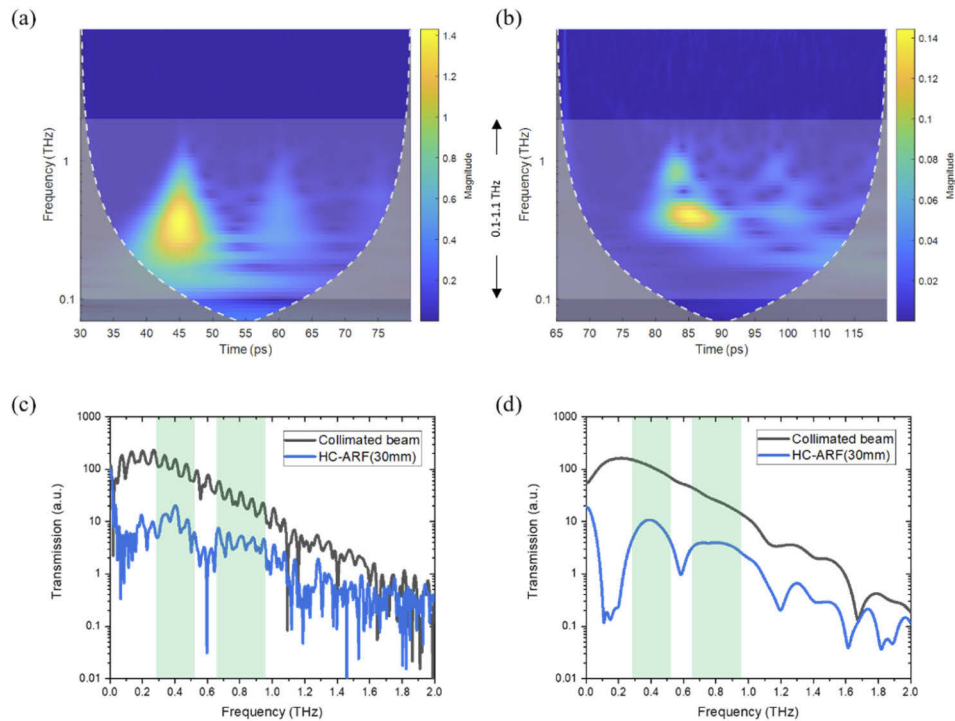


**Fig. 6.** (a) Scalogram from continuous wavelet transform of the THz wave from the THz emitter and (b) transmitted through 30 mm of HC-ARF. (c) Spectral profile of the THz wave from the emitter (black) and when it is transmitted through the HC-ARF (blue) without applied a time window and (d) with applied a time window. The green shade represents the anti-resonant region.

width at half maximum of the Gaussian curve is set at 10 ps which is related to the pulse of the signal. The Fourier transformed spectrum after time windowing are presented in Fig. 6(d), showing a significant noise reduction and clearer resonance and antiresonance regions.

The fiber propagation loss was measured using the cut-back method: three different lengths of fiber (30, 50, and 70 mm) were manufactured. The transmission of the THz wave through the fibers of different lengths was measured, as shown in Fig. 7(a). In this figure, the transmission spectrum was measured in the effective range of the THz source, which is active at  $f \sim 0.1$ -1.1 THz. The anti-resonant region provided a high transmission signal as shaded in Fig. 7(a), whereas the resonant region provided a lower transmission signal. The transmission signal in the guiding band significantly decreased for increasing fiber lengths. The effect of water vapor absorption [42] can also be observed in this measurement, represented by dashed lines in Fig. 7(a).

To confirm the performance of the fiber, the measured fiber geometry was used to evaluate the loss profile of the fiber. The simulation results are shown in Fig. 7(b) (blue line), compared to the experimental values recorded for the extruded HC-ARF (black line): two anti-resonant windows can be clearly observed at the expected spectral regions around  $f \sim 0.42$  and  $f \sim 0.86$  THz, showing the same anti-resonant windows. Although some frequencies have a mismatch between simulation results and experimental results, there is an overall good agreement in terms of loss profile. The attenuation at the anti-resonant frequencies from the experiments  $\sim 3$  dB/m at  $f \sim 0.86$  THz and  $\sim 15$  dB/m at  $f \sim 0.42$  THz is also close to the simulated values. Moreover, the simulation results confirm that the proposed fiber is a single-mode fiber with



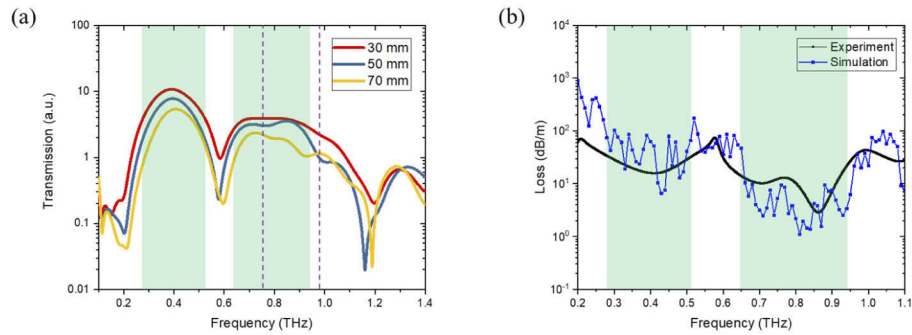


**Fig. 7.** (a) Spectral profile of the THz waves from the HC-ARF with the lengths of 30, 50, and 70 mm where the green windows represent the guiding region and dash lines showing the vapor absorption frequencies. (b) Experimental result and numerical simulation of the attenuation the HC-ARF.

the higher-order-mode extinction ratio (HOMER)  $>18$  at its best, and generally  $>10$  within the frequency range 0.68-0.96THz.

To provide an estimation of bending loss in the fiber, simulations were carried out and are reported in Fig. 8: bend loss is negligible for bending radii larger than 0.4 m. In practice, the fiber used in this work exhibits strong stiffness because of the large diameter (8 mm), thus cannot be bent to radii smaller than 1 m without breaking.

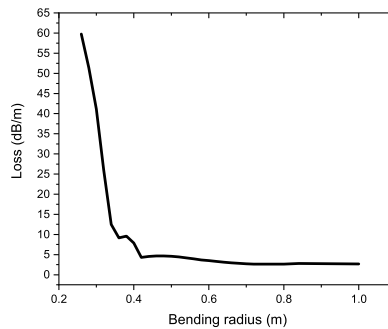


**Fig. 8.** The bending loss as a function of bending radius from the simulation result at 0.86 THz frequency.

## 6. Conclusions

Hollow-core anti-resonant fibers were fabricated by a conventional 3D printer with a structured nozzle specifically manufactured. The fiber attenuation was simulated and optimized in the region of interest at  $f=0.9$  THz by optimizing the fiber cross sectional profile. The core perimetral wall thickness plays an important role in determining the transmission bands, while strut thickness and core diameter improve the confinement loss. The optimized parameters were used to design the nozzle, which was used to manufacture the fiber. The simulation models demonstrated the ability of the fiber to confine THz waves in the air core. Time and frequency domain analysis of the experimental data confirmed air-core guidance with fiber loss of  $\sim 3$  dB/m at  $f \sim 0.86$  THz. This model able to improve the efficiency from the previous work [28] which reduce the loss from  $\sim 12$  dB/m to  $\sim 3$  dB/m and increase the width of transmission window. The loss reported in this work is comparable with the lowest loss reported on the hollow-core THz fiber fabricated from the 3D

printer ( $\sim 3$  dB/m at 0.265 THz) [43]. The improved loss in HC-ARF for THz guiding leading to the wider applications in THz frequency such as biomedical sensing and chemical detection.

**Funding.** Engineering and Physical Sciences Research Council (EPSRC) (EP/P511407/1).

**Acknowledgments.** N. Phanchat gratefully acknowledge the financial support from the Development and Promotion of Science and Technology Talents Project (Royal Thai Government scholarship). W. Talataisong acknowledge funding support from the NSRF via the Program Management Unit for Human Resources & Institutional Development, Research and Innovation [grant number B05F640051].

**Disclosures.** The authors declare no conflicts of interest.

**Data availability.** Data underlying the results presented in this paper are not publicly available at this time but may be obtained from the authors upon reasonable request.

## References

1. J. F. Federici, B. Schulkin, F. Huang, D. Gary, R. Barat, F. Oliveira, and D. Zimdars, "THz imaging and sensing for security applications—explosives, weapons and drugs," *Semicond. Sci. Technol.* **20**(7), S266–S280 (2005).
2. G. C. Trichopoulos, H. L. Mosbacker, D. Burdette, and K. Sertel, "A Broadband Focal Plane Array Camera for Real-time THz Imaging Applications," *IEEE Trans. Antennas Propag.* **61**(4), 1733–1740 (2013).
3. E. V. Yakovlev, K. I. Zaytsev, I. N. Dolganova, and S. O. Yurchenko, "Non-Destructive Evaluation of Polymer Composite Materials at the Manufacturing Stage Using Terahertz Pulsed Spectroscopy," *IEEE Trans. Terahertz Sci. Technol.* **5**(5), 810–816 (2015).
4. D. M. Mittleman, "Twenty years of terahertz imaging [Invited]," *Opt. Express* **26**(8), 9417–9431 (2018).
5. M. Zhang and J. T. W. Yeow, "Nanotechnology-Based Terahertz Biological Sensing: A review of its current state and things to come," *IEEE Nanotechnology Mag.* **10**(3), 30–38 (2016).
6. M. Borovkova, M. Khodzitsky, P. Demchenko, O. Cherkasova, A. Popov, and I. Meglinski, "Terahertz time-domain spectroscopy for non-invasive assessment of water content in biological samples," *Biomed. Opt. Express* **9**(5), 2266–2276 (2018).
7. K. Wang and D. M. Mittleman, "Metal wires for terahertz wave guiding," *Nature* **432**(7015), 376–379 (2004).
8. M. S. Islam, J. Sultana, K. Ahmed, M. R. Islam, A. Dinovtser, B. W. Ng, and D. Abbott, "A Novel Approach for Spectroscopic Chemical Identification Using Photonic Crystal Fiber in the Terahertz Regime," *IEEE Sens. J.* **18**(2), 575–582 (2018).
9. D. F. Swearer, S. Gottheim, J. G. Simmons, D. J. Phillips, M. J. Kale, M. J. McClain, P. Christopher, N. J. Halas, and H. O. Everitt, "Monitoring Chemical Reactions with Terahertz Rotational Spectroscopy," *ACS Photonics* **5**(8), 3097–3106 (2018).
10. P. Doradla, C. Joseph, and R. H. Giles, "Terahertz endoscopic imaging for colorectal cancer detection: Current status and future perspectives," *WJGE* **9**(8), 346–358 (2017).
11. P. H. Siegel, "THz Instruments for Space," *IEEE Trans. Antennas Propag.* **55**(11), 2957–2965 (2007).
12. I. F. Akyildiz, J. M. Jornet, and C. Han, "Terahertz band: Next frontier for wireless communications," *Physical Communication* **12**, 16–32 (2014).
13. S. U. Hwu, K. B. deSilva, and C. T. Jih, "Terahertz (THz) wireless systems for space applications," in 2013 *IEEE Sensors Applications Symposium Proceedings* (2013), pp. 171–175.
14. R. Khabibullin, D. Ushakov, A. Afonenko, N. Shchavruk, D. Ponomarev, O. Volkov, V. Pavlovskiy, I. Vasil'evskii, D. Safonov, and A. Dubinov, "Silver-based double metal waveguide for terahertz quantum cascade laser," *Proc. SPIE* **11022**, 35 (2019).
15. B. You and J. Lu, "Remote and in situ sensing products in chemical reaction using a flexible terahertz pipe waveguide," *Opt. Express* **24**(16), 18013–18023 (2016).
16. G. C. Trichopoulos and K. Sertel, "Polarimetric terahertz probe for endoscopic assessment of malignancies," in 2015 *IEEE International Symposium on Antennas and Propagation & USNC/URSI National Radio Science Meeting* (2015), pp. 730–731.
17. C.-H. Lai, B. You, j. Y. Lu, T. A. Liu, J.-L. Peng, C.-K. Sun, and H.-c. Chang, "Modal characteristics of anti-resonant reflecting pipe waveguides for terahertz waveguiding," *Opt. Express* **18**(1), 309–322 (2010).
18. R. Mendis and D. Grischkowsky, "Plastic ribbon THz waveguides," *J. Appl. Phys.* **88**(7), 4449–4451 (2000).
19. H. Han, H. Park, M. Cho, and J. Kim, "Terahertz pulse propagation in a plastic photonic crystal fiber," *Appl. Phys. Lett.* **80**(15), 2634–2636 (2002).
20. M. Goto, A. Quema, H. Takahashi, S. Ono, and N. Sarukura, "Teflon Photonic Crystal Fiber as Terahertz Waveguide," *Jpn. J. Appl. Phys.* **43**(2B), L317–L319 (2004).
21. Q. Chen, W. Zhu, D. Kong, X. He, B. Li, J. Miao, Z. Luo, X. Zhou, C. Yang, and J. Zhang, "Development of 2.5THz suspended porous microstructured fiber based on cyclic-olefin copolymer," *Optik* **145**, 56–60 (2017).
22. M. S. Islam, J. Sultana, J. Atai, D. Abbott, S. Rana, and M. R. Islam, "Ultra low-loss hybrid core porous fiber for broadband applications," *Appl. Opt.* **56**(4), 1232–1237 (2017).
23. K. Nielsen, H. K. Rasmussen, A. J. L. Adam, P. C. M. Planken, O. Bang, and P. U. Jepsen, "Bendable, low-loss Topas fibers for the terahertz frequency range," *Opt. Express* **17**(10), 8592–8601 (2009).

24. Q. Chen, Y. Zhang, X. He, D. Kong, and J. Zhang, "Design and fabrication of Cyclic-olefin Copolymer based terahertz hollow-core photonic crystal fiber," in 2013 *38th International Conference on Infrared, Millimeter, and Terahertz Waves (IRMMW-THz)* (2013), pp. 1–2
25. S. Yan, S. Lou, X. Wang, T. Zhao, and W. Zhang, "High-birefringence hollow-core anti-resonant THz fiber," *Opt. Quantum Electron.* **50**(3), 162 (2018).
26. S. Yang, X. Sheng, G. Zhao, S. Lou, and J. Guo, "3D Printed Effective Single-Mode Terahertz Antiresonant Hollow Core Fiber," *IEEE Access* **9**, 29599–29608 (2021).
27. W. Talataisong, J. Gorecki, R. Ismaeel, M. Beresna, D. Schwendemann, V. Apostolopoulos, and G. Brambilla, "Singlemoded THz guidance in bendable TOPAS suspended-core fiber directly drawn from a 3D printer," *Sci. Rep.* **10**(1), 11045 (2020).
28. W. Talataisong, J. Gorecki, L. D. Putten, R. Ismaeel, J. Williamson, K. Addinall, D. Schwendemann, M. Beresna, V. Apostolopoulos, and G. Brambilla, "Hollow-core antiresonant terahertz fiber-based TOPAS extruded from a 3D printer using a metal 3D printed nozzle," *Photon. Res.* **9**(8), 1513–1521 (2021).
29. N. Phanchat and R. Chitaree, "The design of high birefringence hollow core with nested anti-resonance nodeless fiber," *Proc. SPIE* **11331**, 113310 T (2020).
30. M. Hou, F. Zhu, Y. Wang, Y. Wang, C. Liao, S. Liu, and P. Lu, "Antiresonant reflecting guidance mechanism in hollow-core fiber for gas pressure sensing," *Opt. Express* **24**(24), 27890–27898 (2016).
31. J. Sultana, M. S. Islam, C. M. B. Cordeiro, M. S. Habib, A. Dinovitser, M. Kaushik, B. W.-H. Ng, H. Ebendorff-Heidepriem, and D. Abbott, "Hollow Core Inhibited Coupled Antiresonant Terahertz Fiber: A Numerical and Experimental Study," *IEEE Trans. Terahertz Sci. Technol.* **11**(3), 245–260 (2021).
32. L. Chen, H. Chen, T. Kao, J. Lu, and C. Sun, "Low-loss subwavelength plastic fiber for terahertz waveguiding," *Opt. Lett.* **31**(3), 308–310 (2006).
33. J. Sultana, M. S. Islam, C. M. B. Cordeiro, M. S. Habib, A. Dinovitser, B. W.-H. Ng, and D. Abbott, "Exploring Low Loss and Single Mode in Antiresonant Tube Lattice Terahertz Fibers," *IEEE Access* **8**, 113309–113317 (2020).
34. S. Atakaramians, S. Afshar V, T. M. Monro, and D. Abbott, "Terahertz dielectric waveguides," *Adv. Opt. Photon.* **5**(2), 169–215 (2013).
35. S. Atakaramians, S. Afshar V, H. Ebendorff-Heidepriem, M. Nagel, B. M. Fischer, D. Abbott, and T. M. Monro, "THz porous fibers: design, fabrication and experimental characterization," *Opt. Express* **17**(16), 14053–14062 (2009).
36. S. F. Busch, M. Weidenbach, J. C. Balzer, and M. Koch, "THz Optics 3D Printed with TOPAS," *J. Infrared, Millimeter, Terahertz Waves* **37**(4), 303–307 (2016).
37. C. S. Ponceca, R. Pobre, E. Estacio, N. Sarukura, A. Argyros, M. C. Large, and M. A. Eijkelenborg, "Transmission of terahertz radiation using a microstructured polymer optical fiber," *Opt. Lett.* **33**(9), 902–904 (2008).
38. J. Y. Shin, J. Y. Park, C. Liu, J. He, and S. C. Kim, "Chemical structure and physical properties of cyclic olefin copolymers (IUPAC Technical Report)," *Pure Appl. Chem.* **77**(5), 801–814 (2005).
39. G. Khanarian, "Optical properties of cyclic olefin copolymers," *Opt. Eng.* **40**(6), 1024 (2001).
40. G. K. M. Hasanuzzaman, S. Iezekiel, C. Markos, and M. S. Habib, "Hollow-core fiber with nested anti-resonant tubes for low-loss THz guidance," *Opt. Commun.* **426**, 477–482 (2018).
41. W. Lu and A. Argyros, "Terahertz Spectroscopy and Imaging With Flexible Tube-Lattice Fiber Probe," *J. Lightwave Technol.* **32**(23), 4621–4627 (2014).
42. Y. Wang, Z. Chen, Z. Zhao, L. Zhang, K. Kang, and Y. Zhang, "Restoration of terahertz signals distorted by atmospheric water vapor absorption," *J. Appl. Phys.* **105**(10), 103105 (2009).
43. Y. Luo, J. Canning, J. Zhang, and G. D. Peng, "Toward optical fibre fabrication using 3D printing technology," *Optical Fiber Technology* **58**, 102299 (2020).